Physics in Medicine & Biology

Wavelength censoring for spectroscopy in optical functional neuroimaging

To cite this article before publication: Brian Richard White *et al* 2020 *Phys. Med. Biol.* in press https://doi.org/10.1088/1361-6560/abd418

Wavelength censoring for spectroscopy in optical functional neuroimaging

Brian R White[1], Jonah A Padawer-Curry[2], Tiffany Ko[2], Wesley Baker[2], Jake Breimann[2], Akiva S Cohen[3], Daniel J Licht[2] and Arjun G Yodh[4]

[1] Division of Pediatric Cardiology, Department of Pediatrics, The Children's Hospital of Philadelphia and The Perelman School of Medicine at the University of Pennsylvania. 3401 Civic Center Blvd., Pediatric Cardiology - 8NW, Philadelphia, PA 19104, USA

[2] Division of Neurology, Department of Pediatrics, The Children's Hospital of Philadelphia and The Perelman School of Medicine at the University of Pennsylvania

[3] Department of Anesthesiology and Critical Care Medicine, The Children's Hospital of Philadelphia. 3615 Civic Center Blvd., Abramson Research Center, Room 816-H, Philadelphia, PA 19104

[4] Department of Physics and Astronomy, University of Pennsylvania, Philadelphia, PA 19104

E-mail: whiteb1@email.chop.edu

Abstract. Optical neuromonitoring provides insight into neurovascular physiology and brain structure and function. These methods rely on spectroscopy to relate light absorption changes to variation of concentrations of physiologic chromophores such as oxy- and deoxyhemoglobin. In clinical or preclinical practice, data quality can vary significantly across wavelengths. In such situations, standard spectroscopic methods may perform poorly, resulting in data loss and limiting field-of-view. To address this issue, and thereby improve the robustness of optical neuromonitoring, we develop, in this manuscript, novel methods to perform spectroscopy even when data quality exhibits wavelength-dependent spatial variation. We sought to understand the impact of spatial, wavelength-based censoring on the physiologic accuracy and utility of hemoglobin spectroscopy. The principles of our analysis are quite general, but to make the methodology tangible we focused on optical intrinsic signal imaging of resting-state functional connectivity in mice. Starting with spectroscopy using four sources, all possible subset spectroscopy matrices were assessed theoretically, using simulated data, and using experimental data. These results were compared against the use of the full spectroscopy matrix to determine which subsets yielded robust results. Our results demonstrated that accurate calculation of changes in hemoglobin concentrations and the resulting functional connectivity network maps was possible even with censoring of some wavelengths. Additionally, we found that the use of changes in total hemoglobin (rather than oxy- or deoxyhemoglobin) yielded results more robust to experimental noise and allowed for the preservation of more data. This new and rigorous image processing method should improve the fidelity of clinical and preclinical functional neuroimaging studies.

Keywords: Optical Neuroimaging, Hemoglobin Spectroscopy, Optical Intrinsic Signal, Functional Connectivity, Signal-to-Noise

Submitted to: *Phys. Med. Biol.*

1. Introduction

Optical neuroimaging and neuromonitoring systems hold promise to provide insight into bedside clinical care and preclinical animal models (White et al. 2012; Bauer et al. 2014; Lynch et al. 2014; Selb et al. 2015; Ko et al. 2018). To fulfill this promise, it is desirable that measurements and analysis be robust to noise and other errors that frequently arise during data acquisition (Yücel et al. 2017; Wheelock et al. 2019). Indeed, many algorithms can generate ideal results in controlled environments but fail in practical scenarios. A crucial step in most optical measurement schemes is spectroscopy, wherein data from multiple wavelengths is analyzed to determine the concentrations of physiologically relevant molecules. Here, we aim to understand how partial data loss (*i.e.*, censoring) affects spectroscopy performance, and we develop a novel algorithm to overcome these problems and recover useable data.

The goal of most optical neuromonitoring systems is to determine concentrations (or relative changes in concentrations) of oxy- and deoxyhemoglobin as well as other chromophores such as water, lipid, and cytochrome oxidase. Since these chromophores have differing absorption spectra, their individual concentrations can be determined from light absorption measurements at multiple wavelengths. However, the accuracy of this spectroscopic calculation is dependent on the particular wavelengths chosen. Multiple methods have been developed to select optimal wavelengths, including search algorithms (Arifler et al. 2015), singular value decomposition (Corlu et al. 2003; Corlu et al. 2005; Brendel and Nielsen 2009; Correia et al. 2010), uniqueness (Corlu et al. 2003; Corlu et al. 2005; Brendel and Nielsen 2009; Correia et al. 2010), and error minimization (Brendel and Nielsen 2009). In these schemes, determination of "optimal" wavelengths relies on the assumption that data from all wavelengths is fully available and is of equal quality.

In practice, quality issues can prevent use of all data at all times. A camera or detector may become saturated at one wavelength and not others, for example, or data at one wavelength may be of poor quality due to hair interfering with fiber contact. For this reason, we developed quality-control metrics that masked data at certain pixels from optical intrinsic signal (OIS) images (White et al. 2019) based on camera saturation as well as signal variance. Similar concepts have been developed to remove source-detector pairs from diffuse optical tomography (DOT) or near-infrared spectroscopy (NIRS) data prior to reconstruction or analysis (White and Culver 2010; Eggebrecht et al. 2012; Ferradal et al. 2016; Pollonini et al. 2016; Hocke et al. 2018). In practice, such masks are wavelength-specific (*e.g.*, pixels may be saturated only at one wavelength). The current state-of-the-art in optical imaging allows spectroscopy

only when all wavelengths are available; even loss of data at one wavelength renders the remaining data at that measurement location useless. Therefore, for OIS, the final mask for oxy- and deoxyhemoglobin will contain only measurements within the intersection of masks at all wavelengths. As a result, large decreases in the field-of-view often arise. For the case of DOT or NIRS, wherein images are obtained using topographic or tomographic reconstruction algorithms, missing wavelengths will result in statistical errors and missing data. Thus, new algorithms are needed to address these spectroscopic problems that affect all optical neuromonitoring systems that rely on multiple wavelengths for chromophore analysis.

In this contribution, we develop a novel methodology, termed *wavelength censored spectroscopy*, that overcomes these problems and thereby enables experimenters to perform spectroscopy even when data from only a subset of wavelengths is available. We, then, seek to understand under what conditions the results of this new algorithm are accurate and reliable. In order to ground our approach, we will focus on simulated and experimental data from an optical intrinsic signal (OIS) neuroimaging system designed to measure changes of the concentrations of oxy- , deoxy-, and total hemoglobin ($\Delta[\mathrm{HbO}_2]$, $\Delta[\mathrm{Hb}_\mathrm{R}]$, and $\Delta[\mathrm{Hb}_\mathrm{T}]$, respectively) in the brains of mice. Two objectives underlie our wavelength censoring approach. First, we will examine the error in the calculation of changes in hemoglobin concentrations that arises from performing spectroscopy using different wavelength subsets. As we expect that certain wavelength combinations would perform poorly compared to the full spectroscopy matrix, a look-up table of allowable wavelength combinations could (in principle) be created to indicate which data could be used for analysis despite censored wavelengths. Second, we examine the effects of experimental noise and spectroscopic error on our ability to generate useable functional neuroimaging data. For this analysis, we will use simulated and experimental resting-state functional connectivity data. Functional connectivity is performed by correlating hemodynamic time series at different cortical locations in order to map neuronal networks. Optical measurements of resting-state functional connectivity networks in mice have provided unique insights into disease pathology such as Alzheimer's disease (Bero et al. 2012) and stroke (Bauer et al. 2014). The approaches described herein, however, are generalizable to the majority of optical functional neuroimaging and neuromonitoring approaches, including near-infrared spectroscopy (NIRS) and diffuse optical tomography (DOT). Previous optical functional connectivity analyses have shown that maps generated with different hemoglobin species show equivalent functional connectivity structure (White et al. 2009; Kura et al. 2018). However, as noise in the reconstructed time series leads to artificially low correlation coefficients (biasing functional connectivity calculations), we predict that experimental noise and the need to censor data from varying wavelengths will differentially affect the practical ability of each contrast to reveal the expected connectivity structure. In this manuscript, we present results from a theoretical analysis of the spectroscopy matrix, from simulated data, and from experimental data that explore these objectives and aid the development of best practices.

2. Methods

2.1. Optical Intrinsic Signal Imaging System

We performed optical intrinsic signal (OIS) imaging using a system similar to that described previously (White et al. 2019) (Figure 1A). Illumination is derived from four visible-light light emitting diodes (LEDs) with emission spectra nominally centered at 470 nm (M470L3-C1), 530 nm (M530L3-C1), 590 nm (M590L3-C1), and 625 nm (M625L3-C1, all from Thorlabs). These wavelengths were chosen from amongst commercially-available visible-light LEDs using the wavelength selection methods of Corlu et al. (2003), Corlu et al. (2005), and Brendel and Nielsen (2009) described below (Section 2.6), such that the four LEDs would together have good spectroscopic performance. Images were acquired with a cooled, CCD camera (iXon 887, Andor Technologies) at 120 Hz. Illumination of each LED was temporally multiplexed such that images at each of the four wavelengths were acquired sequentially; thus, the overall framerate was 30 Hz. Crossed polarizers were used to eliminate light signal from specular reflection. The system was controlled with custom-written software using Matlab and the Andor software development kit.

2.2. Animal Preparation and Imaging

All procedures were approved by the institutional animal care and use committee (IACUC) at the Children's Hospital of Philadelphia (CHOP). Male C57bl/6 mice (ages 8 to 13 weeks) were anesthetized with a mixture of ketamine (100 mg/kg) and xylazine (10 mg/kg) through intraperitoneal injection. After achieving adequate anesthesia, the animal was held in place with ear bars and was kept warm with a heating pad. The hair on the dorsal surface of the head was removed with a depilatory cream, and the scalp was cleaned with iodine and ethyl alcohol. The scalp was incised and reflected to expose the skull from the olfactory bulb (anteriorly) to the superior colliculus (posteriorly) with as much lateral exposure as possible. A glass intact-skull cranial window was placed using transparent dental cement (Silasi et al. 2016) (Figure 1B). Note that with the chosen wavelengths and this imaging geometry, the penetration depth is approximately 1 mm such that the images are reflective of the cortical gray matter.

All functional neuroimaging data was acquired during the "resting state" (*i.e.,* no external stimuli were applied) in order to subsequently perform functional connectivity analysis. Tme series imaging data was acquired in 5-minute imaging runs with up to 30 minutes of total imaging time per mouse per session. Data from the camera consists of a series of images of light intensity over time. The two-dimensional images cover the dorsal surface of the mouse brain and surrounding tissue (Figure 1B); the x-direction indicates right-to-left and the y-direction posterior-to-anterior. The field-of-view of the camera was about 1.5 cm (sampled by 128 pixels) along both x and y directions.

The data for each LED, j, was analyzed as normalized changes in measured light

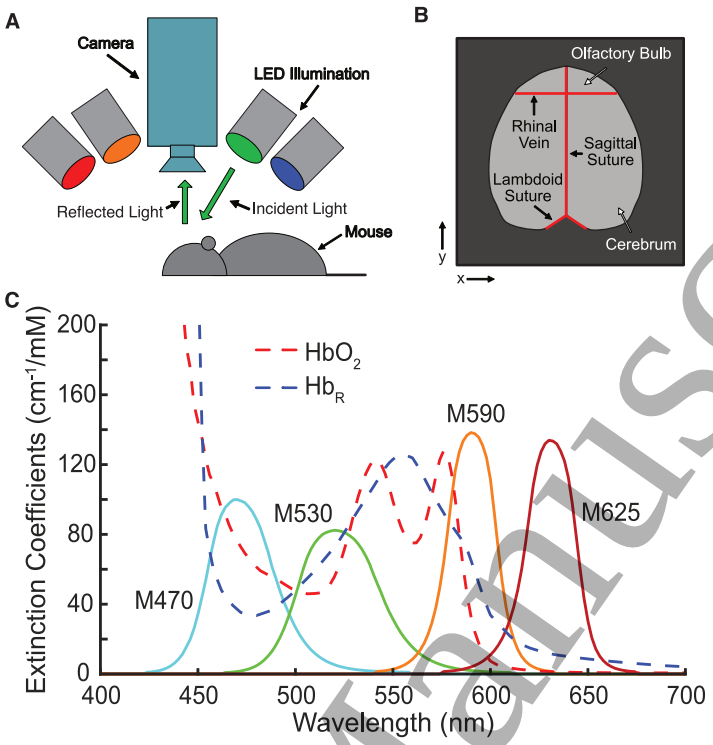

Figure 1. Schematic of the optical intrinsic signal (OIS) imaging system. (A) Diagram of system components. (B) Schematic of the field-of-view: the brain seen through the cranial window and skull is shown in light gray, with surrounding hair and skin in dark gray. Major suture landmarks are shown in red. (C) Experimentally measured spectra for the illuminating light emitting diodes (LEDs) overlaid for comparison with the extinction coefficients for oxy- (HbO_2) and deoxyhemoglobin (Hb_R) (y-axis for LED spectra is arbitrary; heights were normalized to preserve equal area under the curve).

intensity, $I(x, y, t)$, at each pixel position and over time using the Rytov approximation:

$$\Delta I_j(x, y, t) = -\ln\left(\frac{I(x, y, t)}{\langle I(x, y, t)\rangle}\right). \quad (1)$$

These measured changes, $\Delta I(x, y, t)$, are termed *log-ratio* data; the brackets, $\langle\rangle$, denote the temporal mean over the five-minute imaging run. Pixels were masked individually for each wavelength based on quality control criteria as described previously (White et al. 2019). Additional image processing, including segmentation and filtering were performed using standard methods (White et al. 2011; White et al. 2019).

2.3. Spectroscopy Matrix and Mean Path Lengths

For each LED, j, source spectra were measured with a spectrometer (FLAME-S-VIS-NIR-ES, Ocean Optics) and then divided by the area under the spectrum's curve to yield normalized LED source spectra, $S_j(\lambda)$. Measured LED peak wavelengths and full-widths-at-half-maxima deviated slightly from the nominal values (Figure 1C). Hereafter, LEDs will be referred to by their part numbers (*e.g.*, M470). A matrix of extinction

coefficients was constructed using these source spectra and the hemoglobin extinction coefficients, $\epsilon_i(\lambda)$, from Prahl (2002), where i denotes either oxyhemoglobin (HbO_2) or deoxyhemoglobin (Hb_R). For each chromophore, i, and LED, j, a weighted, source-dependent extinction coefficient was determined as:

$$\hat{\epsilon}_{i,j} = \sum_{\lambda} \epsilon_i(\lambda) S_j(\lambda). \tag{2}$$

The matrix of weighted, source-dependent extinction coefficients was then defined as

$$\mathbf{E} = \begin{bmatrix} \hat{\epsilon}_{\mathrm{HbO_2,M470}} & \hat{\epsilon}_{\mathrm{Hb_R,M470}} \\ \hat{\epsilon}_{\mathrm{HbO_2,M530}} & \hat{\epsilon}_{\mathrm{Hb_R,M530}} \\ \hat{\epsilon}_{\mathrm{HbO_2,M590}} & \hat{\epsilon}_{\mathrm{Hb_R,M590}} \\ \hat{\epsilon}_{\mathrm{HbO_2,M625}} & \hat{\epsilon}_{\mathrm{Hb_R,M625}} \end{bmatrix}. \tag{3}$$

A modified Beer-Lambert law (for light from each LED, j) relates log-ratio data to optical tissue absorption changes ($\Delta\mu_{a,j}(x,y,t)$):

$$\Delta I_j(x,y,t) = \Delta\mu_{a,j}(x,y,t) L_j. \tag{4}$$

Here, the mean pathlengths in tissue, L_j, were calculated using the analytical solution to the diffusion approximation of the radiative transfer equation in a semi-infinite geometry (Arridge et al. 1992; White et al. 2011):

$$L_j = \frac{c}{\mu_s'} \times \frac{1}{2\gamma\sqrt{\mu_a c}} \times \left(1 + \frac{3}{c}\mu_a\gamma^2\right) \tag{5}$$

Here, $\gamma = \sqrt{\frac{c}{3(\mu_s'+\mu_a)}}$, and c is the speed of light in tissue. We used an assumed reduced scattered coefficient ($\mu_s' = 10/\mathrm{cm}$), an absorption coefficient calculated from the source-dependent extinction coefficients with an assumed baseline hemoglobin concentration and oxygen saturation ($[\mathrm{Hb_T}]_0 = 76\ \mu\mathrm{M}$ and $\mathrm{S_tO_2}= 65\%$), and an assumed tissue index of refraction (Strangman et al. 2003).

Then, we assumed oxy- and deoxy-hemoglobin are the only chromophores with temporal variance to arrive at the spectroscopy equation:

$$\begin{bmatrix} \Delta\mu_{a,\mathrm{M470}}(x,y,t) \\ \Delta\mu_{a,\mathrm{M530}}(x,y,t) \\ \Delta\mu_{a,\mathrm{M590}}(x,y,t) \\ \Delta\mu_{a,\mathrm{M625}}(x,y,t) \end{bmatrix} = \begin{bmatrix} \hat{\epsilon}_{\mathrm{HbO_2,M470}} & \hat{\epsilon}_{\mathrm{Hb_R,M470}} \\ \hat{\epsilon}_{\mathrm{HbO_2,M530}} & \hat{\epsilon}_{\mathrm{Hb_R,M530}} \\ \hat{\epsilon}_{\mathrm{HbO_2,M590}} & \hat{\epsilon}_{\mathrm{Hb_R,M590}} \\ \hat{\epsilon}_{\mathrm{HbO_2,M625}} & \hat{\epsilon}_{\mathrm{Hb_R,M625}} \end{bmatrix} \begin{bmatrix} \Delta[\mathrm{HbO_2}](x,y,t) \\ \Delta[\mathrm{Hb_R}](x,y,t) \end{bmatrix}; \tag{6}$$

$$\boldsymbol{\Delta\mu_a}(x,y,t) = \mathbf{E} \times \boldsymbol{\Delta}[\mathbf{Hb}](x,y,t). \tag{7}$$

2.4. Simulated Data

In order to understand the effect of noise on spectroscopy in a controlled environment, we first used simulated data. Our goal was to create a model system that would have the similar network properties to resting-state functional connectivity networks. Thus we started with a 100-by-100 pixel image that we divided into sixteen 25-by-25 pixel

regions. As in the brain, the time course for each region consisted of a weight sum of a regional signal as well as a global signal:

$$X_r(t) = G(t) + \alpha R_r(t), \tag{8}$$

where r denotes the region ($r \in \{1, \ldots, 16\}$), $G(t)$ is the *global signal*, $R_r(t)$ is the *regional signal*, and $X_r(t)$ is the final time trace for the region. α is a constant assumed to be 0.5. Both $G(t)$ and all of the $R_r(t)$ were time series of 300 normally-distributed random numbers.

In order to create a network structure, regional signals were chosen such that some regions were correlated and anticorrelated. Namely, each region was correlated with the "homotopic" region on opposite side of the midline ($R_r = R_p$) and anti-correlated with one other region in the same "hemisphere" ($R_r = -R_q$), where r, p, and q are different region labels. Thus, there were four independent regional signals such that every pixel would be correlated with pixels in its own region and those in the homotopic region, and each pixel was anticorrelated with pixels in two regions (one ipsilateral and one contralateral).

Simulated signals were then converted into simulated changes in oxy- and deoxyhemoglobin as:

$$\Delta[\mathrm{HbO_2}]_i(t) = \beta X_i(t) \mathrm{S_tO_{2,0}}[\mathrm{Hb_T}]_0, \tag{9}$$

$$\Delta[\mathrm{Hb_R}]_i(t) \quad = \gamma \Delta[\mathrm{HbO_2}]_i(t). \tag{10}$$

For the baseline total hemoglobin concentration, $[\mathrm{Hb_T}]_0$, and tissue oxygen saturation, $\mathrm{S_tO_{2,0}}$, the values from Strangman et al. (2003) were used, as in Section 2.3. Changes in oxyhemoglobin from the global signal were set to be 10% of baseline ($\beta = 0.1$). Changes in deoxyhemoglobin were assumed to be anti-correlated with, and half the magnitude of, changes in oxyhemoglobin ($\gamma = -0.5$). These assumptions are based off of previous literature on neurovascular coupling (Raichle 2010; Hillman 2014; Bergonzi et al. 2015). (Note: we did perform a sensitivity analysis to test whether our later results were due to these asumptions, see Section 2.7.) Absorption changes were computed from these concentration changes and then converted to simulated changes in the log-ratio of measured light intensity, $\Delta I(x, y, t)$, using the spectroscopy matrix and mean optical pathlengths. The above assumptions resulted in variance in the log-ratio data that was similar to that observed experimentally.

2.5. Wavelength Censored Spectroscopy

As defined above, spectroscopy relates how changes in absorption at each LED are determined by changes in oxy- and deoxyhemoglobin concentrations via the system of linear equations, $\boldsymbol{\Delta\mu_a}(x, y, t) = \mathbf{E} \times \boldsymbol{\Delta}[\mathbf{Hb}](x, y, t)$. These equations can be solved using ordinary least squares techniques, $\boldsymbol{\Delta}[\mathbf{Hb}](x, y, t) = (\mathbf{E}^T\mathbf{E})^{-1}\mathbf{E}^T\boldsymbol{\Delta\mu_a}(x, y, t)$, which minimize the error $\|\boldsymbol{\Delta\mu_a}(x, y, t) - \mathbf{E}\boldsymbol{\Delta}[\mathbf{Hb}](x, y, t)\|^2$.

This process assumes that data is available for all LEDs. To account for missing data from censored LED data, we must adjust the above equation. Let $\mathbf{W}$, the *censoring matrix*, be a diagonal matrix:

$$\mathbf{W} = \begin{bmatrix} w_1 & 0 & 0 & 0 \\ 0 & w_2 & 0 & 0 \\ 0 & 0 & w_3 & 0 \\ 0 & 0 & 0 & w_4 \end{bmatrix}, \tag{11}$$

where w_i is 1 if data from LED i is present, and 0 if not. Note that $\mathbf{W}$ is spatially variant, $\mathbf{W}(x, y)$, as the coefficients along the diagonal vary with position based on data quality metrics. The *censored form* of the spectroscopy equation is then:

$$\mathbf{W}(x, y) \times \boldsymbol{\Delta\mu_a}(x, y, t) = \mathbf{W}(x, y) \times \mathbf{E} \times \boldsymbol{\Delta}[\mathbf{Hb}](x, y, t). \tag{12}$$

Then, the ordinary least squares inversion is:

$$\boldsymbol{\Delta}[\mathbf{Hb}](x, y, t) = \left((\mathbf{W}(x, y)\mathbf{E})^T \mathbf{W}(x, y)\mathbf{E}\right)^{-1} (\mathbf{W}(x, y)\mathbf{E})^T \mathbf{W}(x, y)\boldsymbol{\Delta\mu_a}(x, y, t). \tag{13}$$

We define $\tilde{\mathbf{E}}(x, y) = \mathbf{W}(x, y)\mathbf{E}$, and rewrite this equation:

$$\boldsymbol{\Delta}[\mathbf{Hb}](x, y, t) = \left(\tilde{\mathbf{E}}(x, y)^T \tilde{\mathbf{E}}(x, y)\right)^{-1} \tilde{\mathbf{E}}(x, y)^T \mathbf{W}(x, y)\boldsymbol{\Delta\mu_a}(x, y, t). \tag{14}$$

Note, spatial variance is now incorporated into the spectroscopy matrix, $\tilde{\mathbf{E}}(x, y)$. This expression minimizes the error:

$$\|\mathbf{W}(x, y)\boldsymbol{\Delta\mu_a}(x, y, t) - \mathbf{W}(x, y)\mathbf{E}\boldsymbol{\Delta}[\mathbf{Hb}](x, y, t)\|^2 \tag{15}$$

$$= \left\|\mathbf{W}(x, y)\boldsymbol{\Delta\mu_a}(x, y, t) - \tilde{\mathbf{E}}(\mathbf{x}, \mathbf{y})\boldsymbol{\Delta}[\mathbf{Hb}](x, y, t)\right\|^2. \tag{16}$$

We term this technique *wavelength censored spectroscopy.*

2.6. Assessment of Spectroscopy Matrix Quality

The constructions described above permit spectroscopy to be performed with a subset of the original data. However, it is not clear whether the results will be equivalent to those obtained with the full matrix, in particular, if applied in the presence of physiologic and experimental noise. Although we selected the original complement of four LEDs to optimize spectroscopic performance, the censored matrices, using only subsets of the original sources, may have performance that varies substantially and may be inadequate for practical use. To this end, we assessed the theoretical quality of all spectroscopy matrices (both the full 4-LED matrix and all possible 3- and 2-LED combinations) with two standard metrics.

The first metric derives from a wavelength-dependent matrix constructed following the methodology of Corlu et al. (2003), Corlu et al. (2005), and Brendel and Nielsen (2009):

$$\mathbf{M} = \begin{bmatrix} \hat{\epsilon}_{\mathrm{HbO_2,M470}}/\lambda_{\mathrm{peak,M470}} & \hat{\epsilon}_{\mathrm{Hb_R,M470}}/\lambda_{\mathrm{peak,M470}} \\ \hat{\epsilon}_{\mathrm{HbO_2,M530}}/\lambda_{\mathrm{peak,M530}} & \hat{\epsilon}_{\mathrm{Hb_R,M530}}/\lambda_{\mathrm{peak,M530}} \\ \hat{\epsilon}_{\mathrm{HbO_2,M590}}/\lambda_{\mathrm{peak,M590}} & \hat{\epsilon}_{\mathrm{Hb_R,M590}}/\lambda_{\mathrm{peak,M590}} \\ \hat{\epsilon}_{\mathrm{HbO_2,M625}}/\lambda_{\mathrm{peak,M625}} & \hat{\epsilon}_{\mathrm{Hb_R,M625}}/\lambda_{\mathrm{peak,M625}} \end{bmatrix}, \quad (17)$$

where $\lambda_{\mathrm{peak},j}$ is the empirically measured peak wavelength for each LED. (Note, this wavelength-dependence arises, in part, from a power-law assumption for the scattering coefficient (Corlu et al. 2003).) As before, we define $\tilde{\mathbf{M}} = \mathbf{WM}$. Then, the *residual norm* is:

$$R = \left\| \mathbf{W1} - \tilde{\mathbf{M}}(\tilde{\mathbf{M}}^2\tilde{\mathbf{M}})^{-1}\tilde{\mathbf{M}}^T\mathbf{1} \right\|. \quad (18)$$

Here $\mathbf{1}$ denotes the four-by-four unity matrix. Lower values of R indicate that the matrix is more likely to produce non-unique solutions.

The second metric, κ, is the *condition number* of $\tilde{\mathbf{E}}$ (*i.e.*, the ratio of its maximum to its minimum singular value). Smaller κ values represent more minimized crosstalk and thus ensure more equal sensitivity to all chromophores.

2.7. Assessment of Error with Wavelength Censoring

For simulated data, measurement noise was added for each LED (j) at each pixel: $\Delta I'_j(x,y,t) = \Delta I_j(x,y,t) + a \times N_j(x,y,t)$, where $N(x,y,t)$ was a series of normally-distributed random numbers unique to each pixel, and a is an overall noise level. The fractional noise level (a divided by the temporal standard deviation of ΔI_j) was varied between 0% and 100% depending on the simulated experiment, as described below. Spectroscopy was performed using the full complement of data (all four LEDs) and then with all possible subset combinations of LEDs. The root-mean-square error between the measured hemoglobin time series and the simulated time series was calculated for each pixel. For normalization, all errors were divided by the simulated standard deviation of the global signal (*i.e.*, $\beta \mathrm{S_tO_{2,0}[Hb_T]_0}$). The normalized root-mean-square error was also calculated between data from the subset spectroscopy matrices and data obtained from the full matrix.

To test whether any results using the simulated data were due to the particular assumptions made in constructing the simulated resting-state time trace (*e.g.*, that oxy- and deoxyhemoglobin are anticorrelated), we also assessed whether the error was dependent on the magnitude or direction of changes in $\Delta[\mathrm{HbO_2}]$ and $\Delta[\mathrm{Hb_R}]$. Both $\Delta[\mathrm{HbO_2}]$ and $\Delta[\mathrm{Hb_R}]$ were independently varied between -20% and 20% of baseline ($\mathrm{S_tO_{2,0}[Hb_T]_0}$). Measurements were simulated, and 25% Gaussian measurement noise was added, as above. This process was repeated one thousand times, and the normalized root mean square error was calculated.

For experimental data, since the "true" hemodynamics in the mice were unknown, the root-mean-square error was calculated between the hemodynamic data obtained from subset spectroscopy matrices and data from the full spectroscopy matrix. These errors were normalized by the root-mean-square of the $\Delta[\mathrm{HbO}_2]$ signal measured with four wavelengths.

2.8. Functional Connectivity Analysis

For both simulated and experimental data, resting-state functional connectivity analysis was performed as previously described (White et al. 2011; White et al. 2019). Global signal regression was used. Correlation coefficients and functional connectivity maps were generated using a seed-based analysis. For simulated data, an arbitrary seed from one region in the simulated "brain" was chosen (as all regions were statistically equivalent).

We first examined the effect of wavelength censoring on the simulated data when the censoring matrix was spatially-invariant (*i.e.*, the same subset of wavelengths was available at all pixels). We assessed the the performance of functional connectivity in the face of increasing measurement error. The simulated measurement noise was varied from 0% to 100% in 1% increments. The correlation coefficient was calculated between the seed and a pixel known to be correlated, as well as between the seed and a pixel known to be anti-correlated. This procedure was repeated one hundred times and the average correlation coefficient calculated using Fisher transforms. This procedure was repeated for all subset spectroscopy matrices. Example functional connectivity maps were created at 25% measurement noise.

We next analyzed simulated functional connectivity results assuming spatially-variant wavelength censoring. Namely, we assumed that $\mathbf{W}(x, y)$ included all four LEDs for all points in the simulated "left hemisphere", and included only a subset of LEDs for all points in the "right hemisphere". The above analyses demonstrating the response to noise were repeated, and the example functional connectivity networks maps were constructed for all possible right-hemisphere censoring matrices.

For experimental data, we took the same approach. We initially examined spatially-invariant wavelength censoring, and then we examined the effect of different wavelength subsets in the two hemispheres. To perform this analysis, we used data sets which contained high quality data for all LEDs across the entire field-of-view, such that wavelength censoring could be imposed *post hoc*. For functional connectivity with experimental data, seeds were chosen from canonical functional areas (*e.g.*, the motor and retrosplenial cortices) using the expected cortical locations based on histologic atlases and prior neuroimaging results.

We next assessed the use of wavelength censoring in practical examples where data from some LEDs was unable to be used. First, we used data from one run where the intensity on the M470 LED was intentionally increased to saturate a region of the camera's pixels. This saturation caused the quality mask to exclude a small region of

pixels over the left hemisphere for this one LED. Second, we used data from one run wherein the M625 LED moved half-way through the run due to a loose set screw. This change in the angle of illumination caused a shift in the overall baseline for many pixels such that most of the field-of-view failed the signal-to-noise quality threshold for this LED. Wavelength-censored spectroscopy was used based on the empirical pixel quality masks. Functional connectivity maps were created using seeds, as described above.

2.9. Practical considerations for optimal wavelength selection

As will be demonstrated, censored spectroscopy matrices will vary significantly in their ability to correctly determine chromophore concentrations in the setting of experimental noise. Thus, when constructing a new optical neuromonitoring system, the set of illumination sources whose performance is most robust to data loss is not necessarily the same combination that would result in the "optimal" theoretical performance when all wavelengths are available. Thus, we propose a revision to the methods of Corlu et al. (2003), Corlu et al. (2005), and Brendel and Nielsen (2009) described above in Section 2.6. Namely, we will judge four-source combinations by the *worst* theoretical performance of all possible three-source combinations, again using the residual norm and condition number (*i.e.*, the minimum residual norm and maximum condition number of all three-source subsets).

We examined the theoretical performance of all four-LED combinations possible using visible light LEDs available through ThorLabs; these included the four LEDs in the current system (nominal center wavelengths: 470 nm, 530 nm, 590 nm, and 625 nm) as well as LEDs with nominal center wavelengths of 505 nm and 617 nm. Since we were unable to experimentally confirm the spectra of all such LEDs, the LED spectra were assumed to have a Gaussian shape with a peak at the nominal wavelength and a full-width at half-maximum of 30 nm (note, this FWHM is larger than the nominal value, but in line with that empirically measured on our current LEDs). For each selection of four LEDs, the minimum residual norm and maximum condition number of all three-LED combinations was found. Possible LED selections were then compared to each other using these metrics.

3. Results

3.1. Theoretical Assessment of Spectroscopy Matrix Quality

The full (four-LED) spectroscopy matrix for our OIS system as well as all possible three- and two-LED subsets were assessed using the residual norm, R, and the condition number, κ (Figure 2). The full spectroscopy matrix had a residual norm of 0.46 and a condition number of 15.9. These values compare favorably with values for optimized wavelength selections in the prior literature; for example, compare to Figure 1 in Corlu et al. (2005) and Figure 4 in Brendel and Nielsen (2009).

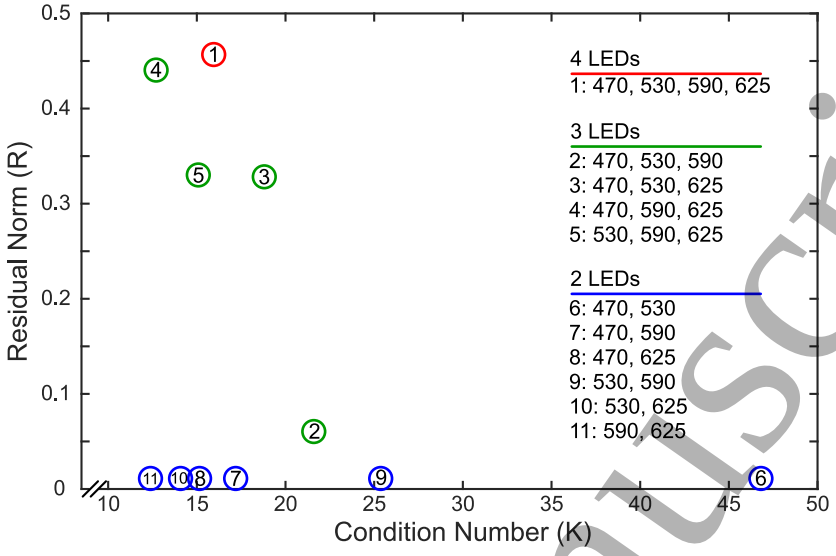

Figure 2. Theoretical assessment of the full spectroscopy matrix (red circle) and all possible sub-matrices (green and blue circles) using condition number (κ, on the x-axis) and residual norm (R, on the y-axis). An ideal matrix would maximize R and minimize κ (*i.e.*, it would be as far to the upper-left as possible). Note the variance in performance of the subset matrices relative to the full matrix. Also, note that all two-LED matrices have a residual norm of zero by definition.

Of the three-LED matrices, three performed well with $R > 0.3$. Interestingly, however, censoring the M625 LED resulted in a residual norm of only $R = 0.06$. All three-LED matrices had excellent condition numbers (κ), with the greatest being 21.6; the three matrices that performed well by R all had $\kappa < 20$ (Figure 2). Note, all two-LED matrices result in $R = 0$, by definition. Thus, these matrices must be judged solely on the basis of their condition number, κ. Four of these matrices had $\kappa < 20$. The matrices that consisted solely of two LEDs with little wavelength separation (*i.e.*, the pairs M470 and M530 as well as M530 and M590) performed poorly with $\kappa > 25$.

3.2. Simulated Optical Intrinsic Signal Data

To test performance with censored spectroscopy matrices, we next analyzed data from the simulated OIS time courses of the 100-by-100 pixel "brain" with 25% added noise. Root-mean-square error was calculated against both the original simulated data (the ground truth) as well as the results attained from the full four-LED spectroscopy matrix. The majority of spectroscopy matrices produced errors for changes in oxy- and deoxyhemoglobin that were comparable in magnitude to the added measurement noise (Table 1). Notably, errors in total hemoglobin concentration changes ($\Delta[\mathrm{Hb_T}]$) were generally less than 10% and were substantially lower than those for $\Delta[\mathrm{HbO_2}]$ and $\Delta[\mathrm{Hb_R}]$ throughout. As expected, differences in performance of the censored matrices were found. The three-LED matrix with the worst performance resulted from censoring the M625 data. Removing this LED resulted in errors in $\Delta[\mathrm{HbO_2}]$ and $\Delta[\mathrm{Hb_R}]$ of

greater than 60% compared to the simulated data. However, censoring the M625 data was not worse than other three-LED combinations when compared to four-LED data. By contrast, censoring the M530 data resulted in measured hemodynamics that were in excellent agreement with data from the full spectroscopy matrix (relative error in $\Delta[HbO_2]$: 2.4%, in $\Delta[Hb_R]$: 2.2%, and in $\Delta[Hb_T]$: 4.6%).

Table 1. Normalized root-mean-square errors (based on simulated data with 25% added measurement noise) for various LED combinations using simulated hemodynamics.

Number of LEDs	LEDs Included	Relative to Simulated Data			Relative to 4 LED Data		
		$\Delta[HbO_2]$	$\Delta[Hb_R]$	$\Delta[Hb_T]$	$\Delta[HbO_2]$	$\Delta[Hb_R]$	$\Delta[Hb_T]$
4 LEDs	M470, M530, M590, M625	39.2%	35.8%	6.9%	-	-	-
3 LEDs	M470, M530, M590	65.7%	60.9%	7.7%	33.3%	31.2%	2.1%
	M470, M530, M625	37.7%	35.7%	7.0%	32.7%	33.3%	0.6%
	M470, M590, M625	39.5%	35.8%	8.4%	2.4%	2.2%	4.6%
	M530, M590, M625	33.6%	37.8%	10.4%	38.1%	29.4%	8.7%
2 LEDs	M470, M530	162%	157%	8.3%	150%	147%	3.6%
	M470, M590	65.7%	60.9%	8.9%	33.3%	31.4%	5.0%
	M470, M625	31.7%	30.0%	9.2%	33.1%	35.6%	5.2%
	M530, M590	105%	91.5%	15.7%	90.0%	76.5%	13.9%
	M530, M625	35.3%	30.6%	10.9%	41.9%	37.1%	9.1%
	M590, M625	44.9%	32.1%	17.9%	57.8%	40.0%	18.3%

As might be expected, fewer of the two-LED matrices performed as well, but this poor performance was limited to $\Delta[HbO_2]$ and $\Delta[Hb_R]$; relative errors in $\Delta[Hb_T]$ were still good throughout. For example, the matrix which involved only the closely-spaced LEDs, M470 and M530, performed particularly poorly based on the condition number. This matrix had the worst errors in $\Delta[HbO_2]$ and $\Delta[Hb_R]$, of over 150% relative to the simulated data; however, its error in $\Delta[Hb_T]$ was only 8.3%.

We next examined the simulated functional connectivity maps (again using 25% added noise): a seed was chosen in one location, and the correlations plotted using $\Delta[HbO_2]$ contrast (Figure 3). In most cases, the expected correlation pattern is present, although the different spectroscopy matrices drastically vary in their ability to recover data without noise. Since the added noise in each pixel is independent, noise in the recovered hemoglobin concentration change is reflected in correlation coefficients that are

closer to zero (no correlation). In particular, for the sub-matrices that performed poorly previously (*e.g.*, the two-LED matrices with closely spaced wavelengths: M470/M530 and M530/M590), the correlation structure is only barely visible. (Images obtained with $\Delta[\mathrm{Hb_R}]$ contrast were similar; data not shown.) We repeated this analysis with $\Delta[\mathrm{Hb_T}]$ contrast (Supplemental Figure 1). The computed functional connectivity networks are much stronger using this contrast, with less sensitivity to noise, as expected from the earlier error analysis. In particular, some of the two-LED subset matrices that performed poorly with $\Delta[\mathrm{HbO_2}]$ provided maps based on $\Delta[\mathrm{Hb_T}]$ contrast that are nearly indistinguishable from those obtained with three or four LEDs.

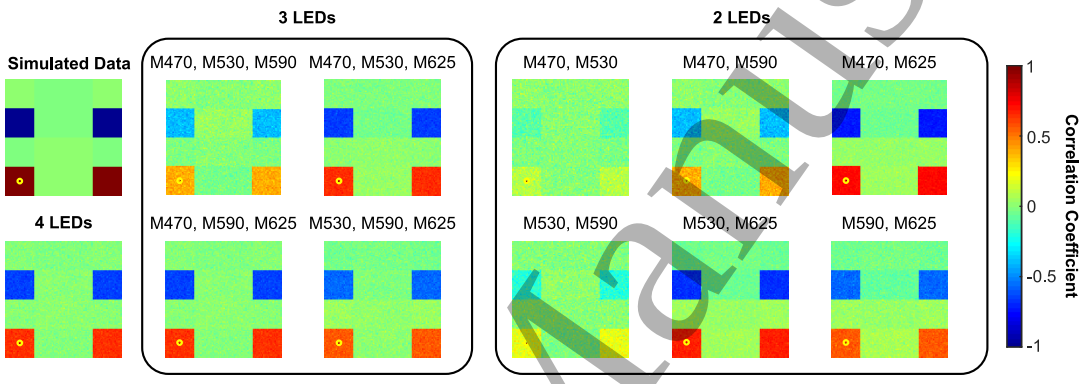

Figure 3. Simulated functional connectivity data analysis with the addition of 25% simulated measurement noise. The seed pixel is in the lower-left region (yellow circle). The simulated data (upper-left subfigure) demonstrates the expected pattern consisting of two correlated regions, two anti-correlated regions, and remaining regions without correlation. Data reconstructions are shown with all possible subset spectroscopy matrices and $\Delta[\mathrm{HbO_2}]$ contrast. Note, the ability to recover expected networks without noise varies between different spectroscopy matrices.

We then examined the effect of increasing noise levels on the performance of functional connectivity correlation analysis. The added noise in the simulated measurements was varied from 0% to 100%. To summarize our findings, we display values of two representative correlations across the range of added noise: a correlation coefficient between the seed pixel and a pixel in the "contralateral" correlated region and the correlation coefficient between the seed pixel and a pixel in the "contralateral" anti-correlated region. At 0% added noise, these correlation coefficients will equal 1 and -1, respectively. As added noise is increased, these values will trend towards 0; the rate of this decay is indicative of the robustness of the spectroscopy matrix to added noise (slower decay being preferred). Results with sub-matrices (three- and two-LED) were compared to the full (four-LED) spectroscopy matrix. Using $\Delta[\mathrm{HbO_2}]$ contrast, the three-LED sub-matrices that performed well in both theoretical tests and error calculations had similar performance to the full matrix (Figure 4, upper-left box). Similar results were possible with the two-LED matrices that had performed well (Figure 4, upper-right box); the two-LED matrices that involved pairs of LEDs with wavelengths closest together (*e.g.*, M470/M530 and M530/M590) had particularly poor

performance; the remaining two matrices had intermediate performance. All results were improved when examining $\Delta[\mathrm{Hb_T}]$ (Figure 4, lower boxes), even for the two wavelength spectroscopy matrices.

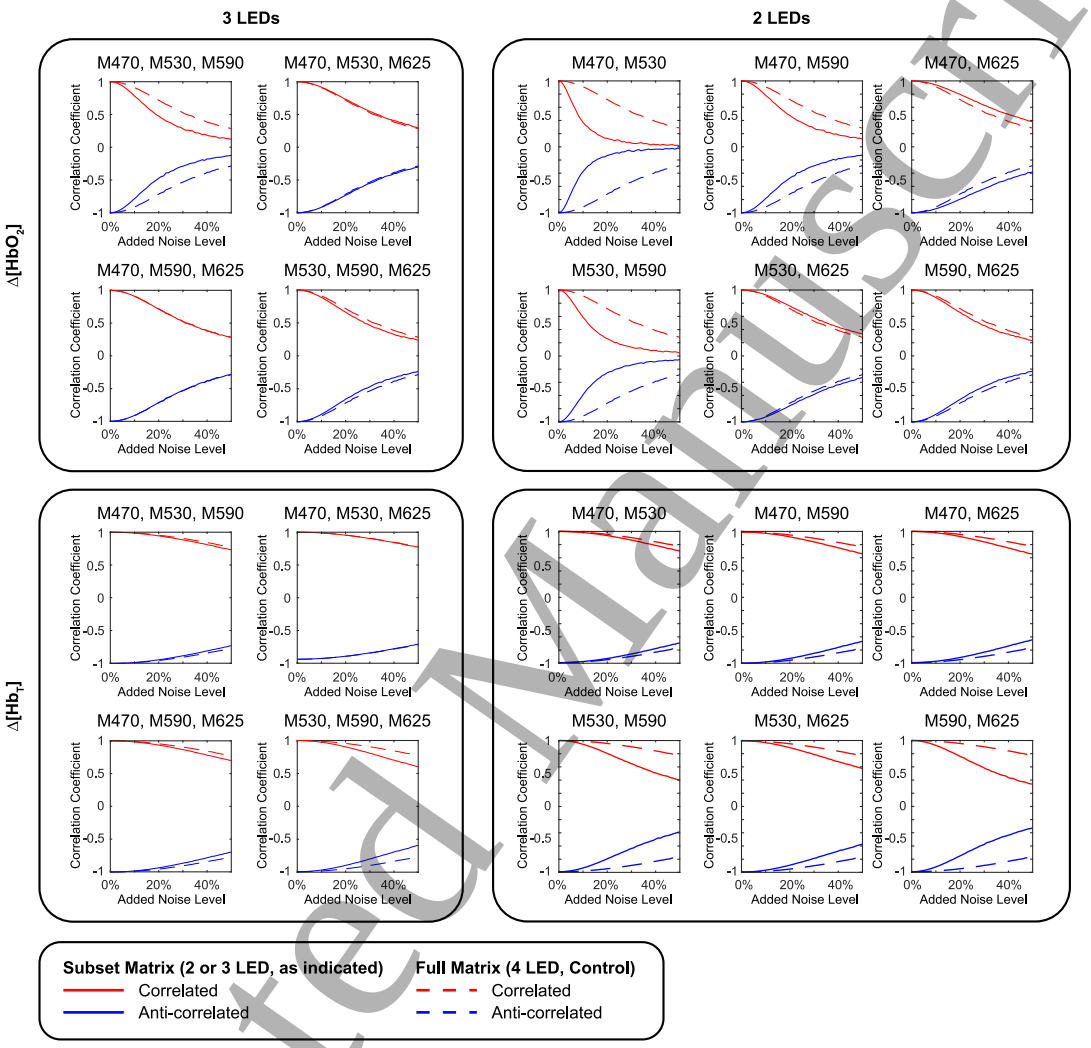

Figure 4. Simulated functional connectivity results with increasing added measurement noise. A 100x100 pixel "brain" was simulated as described. Correlation coefficients are shown between a one pixel seed and two other pixels: a homotopic pixel (correlated, $r = 1$, in red) and a pixel known to be anti-correlated ($r = -1$, in blue). Data from the full, four-wavelength spectroscopy matrix is shown with dashed lines (same in all subfigures). Data from wavelength-censored matrices are grouped by number of wavelengths remaining and are labeled by the remaining wavelengths (solid lines). The top group of subfigures is data using $\Delta[\mathrm{HbO_2}]$ contrast and the lower group is data using $\Delta[\mathrm{Hb_T}]$.

To quantitatively compare the effect of added noise between different subset matrices, we calculated the added noise level at which a particular correlation coefficient fell below $r = 0.75$, compared to the expected $r = 1.0$ in the setting of no added noise (Table 2). These results corroborated those shown in Figure 4. The four-LED

spectroscopy matrix, as well as many of the three-LED and some of the two-LED matrices, were able to determine the correlation values using $\Delta[HbO_2]$ contrast with excellent results up to 20% added noise. However, the two-LED matrices with closely spaced wavelengths performed poorly with $\Delta[HbO_2]$ contrast, wherein noise in the 5-8% range caused drops in correlation coefficients below $r = 0.75$. Use of $\Delta[Hb_T]$ contrast resulted in substantially improved performance with correlation values falling only for noise levels of about 50% for most subset spectroscopy matrices.

Table 2. Performance of correlation analysis in the setting of increasing noise using simulated data. Correlations were calculated between two pixels known to be correlated (*i.e.*, actual $r = 1$). Shown are the level of added measurement noise levels at which data reconstructed with each wavelength combination caused the correlation coefficient to fall below $r = 0.75$ (a higher value of added noise indicates the results were more robust).

Number of LEDs	LEDs Included	Added Noise Level Resulting in $r < 0.75$		
		$\Delta[HbO_2]$	$\Delta[Hb_R]$	$\Delta[Hb_T]$
4 LEDs	M470, M530, M590, M625	20%	11%	57%
3 LEDs	M470, M530, M590	12%	7%	51%
	M470, M530, M625	21%	11%	55%
	M470, M590, M625	20%	11%	47%
	M530, M590, M625	18%	11%	38%
2 LEDs	M470, M530	5%	3%	48%
	M470, M590	12%	7%	44%
	M470, M625	25%	13%	43%
	M530, M590	8%	5%	25%
	M530, M625	22%	13%	36%
	M590, M625	18%	13%	22%

The results above assumed that the censored spectroscopy matrix was spatially-invariant (for example, for the three-LED matrices, the same LED was censored over the entire field-of-view). However, in practice, the censoring matrix will be spatially-variant as pixel-wise quality masking will be LED-dependent. Thus, we simulated a spatially-variant censoring matrix: in the left "hemisphere" of the simulated brain, the full four-LED matrix was used (*i.e.*, no censoring), while in the right "hemisphere" a subset of LEDs was censored (and all possible subset matrices were examined as

before). Results demonstrated that the correlation structure could still be visualized, even though different spectroscopy matrices were used for reconstruction of the data in the two hemispheres (Supplemental Figure 2).

The above results have demonstrated that use of $\Delta[\mathrm{Hb_T}]$ contrast drastically improved the ability of spectroscopy matrices (even those with censoring) to recover the correct changes in hemoglobin concentrations; this finding was true even with high levels of added measurement noise. We suspected that this result might be a consequence of our assumptions in constructing the simulated data, namely that changes in $\Delta[\mathrm{HbO_2}]$ and $\Delta[\mathrm{Hb_R}]$ were anticorrelated and had particular magnitudes relative to the baseline assumed optical properties. To test these hypotheses, we repeated the root-mean-square error analysis from above (Table 1), but we independently varied the changes in $\Delta[\mathrm{HbO_2}]$ and $\Delta[\mathrm{Hb_R}]$ from -20% to 20% of baseline. These results showed that error was independent of the magnitude of changes in either contrast (Supplemental Figure 3). Similarly, it did not appear that lower error in $\Delta[\mathrm{Hb_T}]$ was due to anticorrelation of $\Delta[\mathrm{HbO_2}]$ and $\Delta[\mathrm{Hb_R}]$ since low errors in $\Delta[\mathrm{Hb_T}]$ were seen for all tested changes in $\Delta[\mathrm{HbO_2}]$ and $\Delta[\mathrm{Hb_R}]$, including when these changes had the same sign.

3.3. Experimental Optical Intrinsic Signal Data

We next examined the performance of wavelength censored spectroscopy in experimental data acquired in mice. We first selected runs that contained good data at all LEDs across the field-of-view ($N = 16$). The normalized root-mean-square errors in the ability to calculate $\Delta[\mathrm{HbO_2}]$, $\Delta[\mathrm{Hb_R}]$, and $\Delta[\mathrm{Hb_T}]$ (Table 3) generally followed the patterns found from the simulations with 25% added measurement noise (compare to Table 1, right-hand columns), although the errors in the experiments are slightly larger than in the simulations. The subset matrix with censoring of M530 performed particularly well. The worst errors were seen with the two-wavelength matrices with closely-spaced LEDs. Again, errors were substantially lower in $\Delta[\mathrm{Hb_T}]$ than $\Delta[\mathrm{HbO_2}]$ or $\Delta[\mathrm{Hb_R}]$.

We then examined functional connectivity data from representative five-minute scans using all possible (spatially-invariant) spectroscopy matrices. Seed-based functional connectivity maps with the seed in the left motor (Figure 5) and retrosplenial (Supplemental Figure 4) cortices demonstrated that when using $\Delta[\mathrm{HbO_2}]$, the expected structure was seen with most of the censored spectroscopy matrices. Even with some two LED matrices, the network structure was very similar to that seen using all four LEDs. Two-LED matrices consisting of only of two wavelengths close to each other (*i.e.*, M470/M530 and M530/M590) were most prone to losing correlations due to noise. Maps obtained using $\Delta[\mathrm{Hb_R}]$ were similar (data not shown). As with the simulated data, the use of $\Delta[\mathrm{Hb_T}]$ as a contrast resulted in lower noise and clearer functional connectivity maps (*i.e.*, even with censored matrices that performed poorly with oxyhemoglobin, Figure 6).

Next, we used similar experimental data wherein the original data quality was of excellent in all four LEDs across the entire field-of-view, but in this case we

Table 3. Normalized root-mean-square errors between data calculated with subset spectroscopy matrices and that calculated using the full spectroscopy data. Values were derived from experimental scans ($N = 16$) with the error averaged across pixels within the brain segmentation. Data is shown as the median and interquartile range (IQR) across runs.

Number of LEDs	LEDs Included	Normalized Error Relative to 4 LED Data (%) $\Delta[HbO_2]$	$\Delta[Hb_R]$	$\Delta[Hb_T]$
3 LEDs	M470, M530, M590	58.7 (48.1-65.6)	55.1 (45.2-61.5)	3.6 (3.0-4.1)
	M470, M530, M625	45.6 (41.7-52.7)	46.4 (42.5-53.7)	0.9 (0.8-1.0)
	M470, M590, M625	3.0 (2.8-3.3)	2.7 (2.5-2.9)	5.7 (5.2-6.2)
	M530, M590, M625	57.6 (48.5-61.7)	44.4 (37.4-47.5)	13.2 (11.1-14.1)
2 LEDs	M470, M530	200 (176-219)	195 (172-213)	5.8 (4.8-6.2)
	M470, M590	58.6 (48.1-65.5)	53.6 (44.8-60.7)	7.3 (6.2-7.8)
	M470, M625	56.5 (47.3-64.0)	62.6 (51.5-70.1)	8.1 (6.8-8.7)
	M530, M590	110 (99.6-116)	93.8 (85.1-99.7)	16.6 (15.3-14.1)
	M530, M625	75.4 (61.6-83.6)	65.8 (53.8-73.4)	13.1 (11.1-14.1)
	M590, M625	99.3 (82.8-112)	70.3 (57.8-78.7)	29.7 (25.5-34.1)

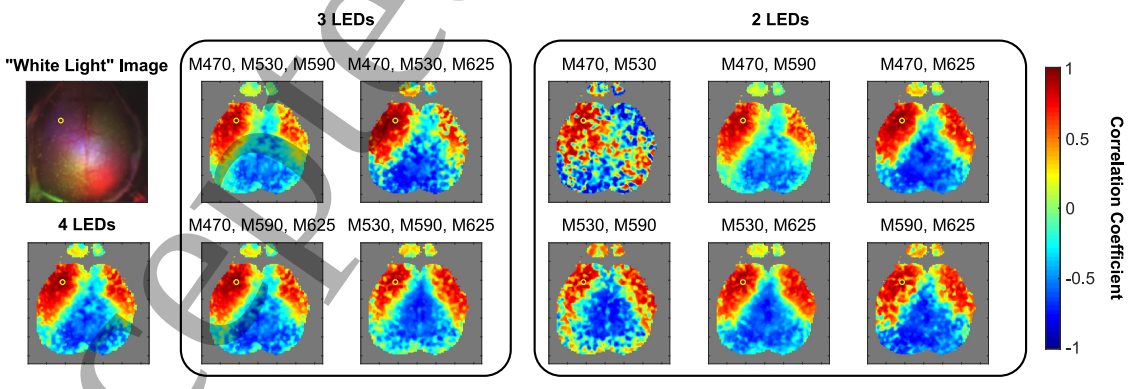

Figure 5. Functional connectivity data with a seed in the left motor cortex (yellow circle) and $\Delta[HbO_2]$ contrast. The expected functional connectivity pattern consists of correlations with the ipsilateral somatosensory cortex as well as homotopic, contralateral motor cortex; these effects are demonstrated using data obtained with four-LED spectroscopy. Data obtained using the censored spectroscopy matrix is shown, with the labels corresponding to the LEDs remaining. The expected functional connectivity network is visible in most of the images, with varying degrees of noise. With some of the two-LED matrices, the correlation structure is lost due to noise.

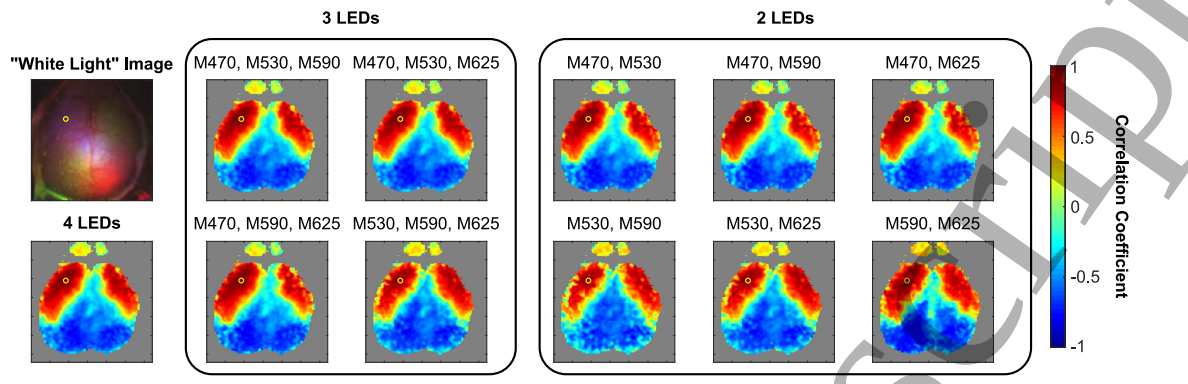

Figure 6. The same functional connectivity maps as in Figure 5, now with $\Delta[\mathrm{Hb_T}]$ contrast. These maps exhibited much lower noise, with the expected functional connectivity structure demonstrated even with censored spectroscopy matrices that previously performed poorly.

assumed that the censoring matrix was spatial variant: namely that the left half of the image (left hemisphere) had a full complement of wavelengths available while the right half (right hemisphere) used a censored spectroscopy matrix. Data from the motor seeds demonstrated that detection of the expected functional connectivity network was possible even with a spatially-variant censoring matrix (Figure 7).

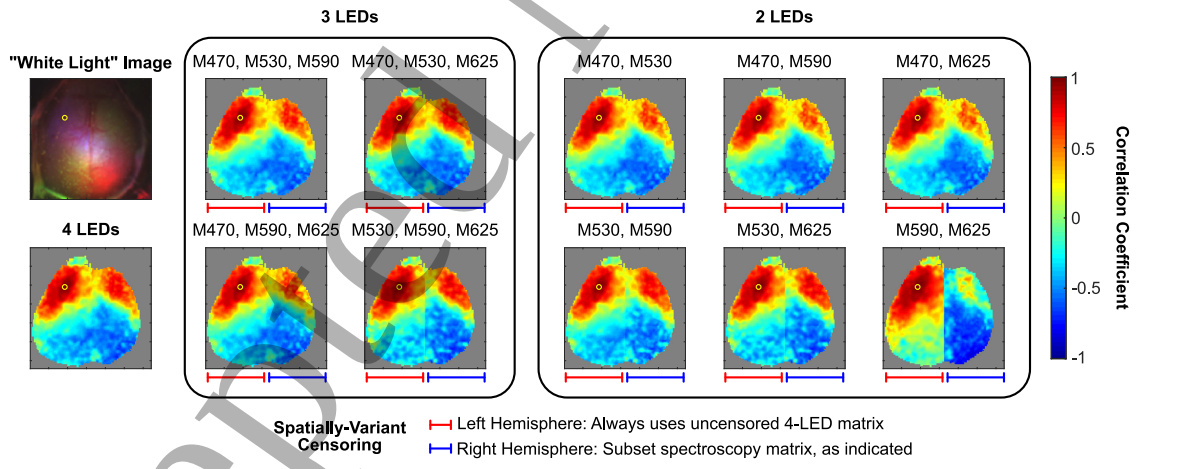

Figure 7. Functional connectivity data with a seed in the left motor cortex (yellow circle) and $\Delta[\mathrm{Hb_T}]$ contrast. The data in the left hemisphere (left half of the image, denoted with the red bracket) was obtained using the full spectroscopy for all images. Data in the right hemisphere (right half of the image, blue bracket) was obtained using the censored spectroscopy matrix, as labeled. In all images (with the exception of M590/M625), the expected pattern was seen.

3.4. Wavelength censoring in practice

In the above analysis, wavelength censoring was imposed *post hoc* on data in which all four LEDs were acquired with good data quality across the entire visible brain. We now examine the use of wavelength censoring on example data where not all LEDs were available across the entire field-of-view. In the first example (Figure 8, top row), the intensity of the M470 LED was intentionally increased to saturate the camera in a region of the left hemisphere. The expected network structure was still visualized (the figure shows the lateral sensorimotor network demonstrated from a seed intentionally chosen from inside the region where only three wavelengths were available). In a second example (Figure 8, bottom row), the set screw holding the M650 LED was loose causing a slight shift in the LED's illumination half-way through the run. Thus, the majority of pixels failed the signal-to-noise quality threshold in this wavelength only. Despite this problem, again we can see the expected lateral sensorimotor network. Without wavelength censoring, all pixels with data less than the full complement of LEDs would have had to be excluded. The field-of-view (especially in Example 2) would be dramatically smaller as a result, and the particular seeds chosen (from within regions with censoring) would not be available for analysis.

3.5. Practical Wavelength Selection

As we have seen, in the setting of wavelength censoring, the performance of the spectroscopy matrix depends both on the initial LEDs chosen and on the performance of the various subset matrices. Therefore, we set out to optimize wavelength selection with the practical consideration that the four LEDs chosen for the system should be judged on the worst performance of any three-LED, censored sub-matrix. All possible four-LED spectroscopy matrices using commercially available visible light LEDs from ThorLabs (Figure 9A) were created. We then calculated the condition number and residual norms for these matrices and all possible three-LED submatrices. Wavelength combinations that had good performance when all wavelengths were available did not necessarily have good performance of their submatrices (Figure 9B). For example, the combination of M470/M505/M530/M617 performed well as a full matrix but particularly poorly when judged based on its subsets. Note, the four LEDs of our current experimental system had good performance of as a full matrix and when censoring one LED.

4. Discussion

In order to be widely applicable and useful, optical neuroimaging and neuromonitoring systems must be robust to the experimental noise and data loss that inevitably arise during routine use. Using traditional spectroscopic methods, noise which results in the inability to use data from one illumination source or wavelength leads to complete data loss. This work provides a rigorous approach to ameliorate such data loss. The efficacy of wavelength censored spectroscopy was demonstrated with both simulated and

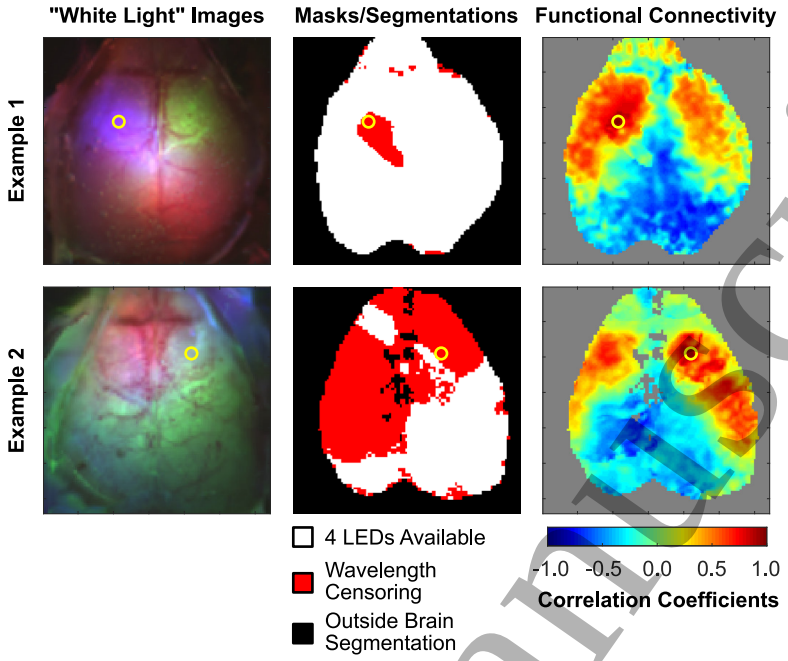

Figure 8. Practical performance of wavelength censoring in example runs with missing data. Two examples are shown. The first column shows false-color images of the mouse brain to demonstrate the landmarks and field-of-view. The seed location for functional connectivity analysis is shown with a yellow circle. The second column demonstrates the pixels included in the analysis after quality masking and manual segmentation. Pixels shown in white had all four LEDs. Pixels in red had less than four LEDs available. Black pixels are outside the brain (*e.g.*, scalp and hair). In the third column, representative functional connectivity maps are shown (both maps use $\Delta[\mathrm{Hb_T}]$ contrast). In example 1 (top row), the M470 LED was intentionally increased in intensity to saturate the camera over a small region in the left hemisphere. In the second example (bottom row), the M650 LED moved slightly half-way through the recording due to a loose set screw. This change in baseline intensity caused a majority of pixels to fail a signal-to-noise threshold for this wavelength. In both cases, the use of spectroscopy with wavelength censoring allows normal delineation of the functional architecture despite choosing a seed from within the region where only three wavelengths are available for analysis. Note: without wavelength censoring, any red pixels in the second column (where data from at least one LED is missing) would have had to be excluded from analysis. In particular, the example seeds chosen would have been outside the usable field-of-view.

experimental data. These results should help improve the field-of-view and utility of optical intrinsic signal imaging (OIS) as well as other neuromonitoring systems, such as near infrared spectroscopy (NIRS) and diffuse optical tomography (DOT).

We examined the variability in the accuracy of subset spectroscopy matrices to accurately calculate changes in concentrations of different hemoglobin species. Results showed that subset illumination combinations varied significantly in their ability to reproduce the expected results. In particular, two-LED combinations consisting solely of closely-spaced wavelengths resulted in the worst relative performance. On the

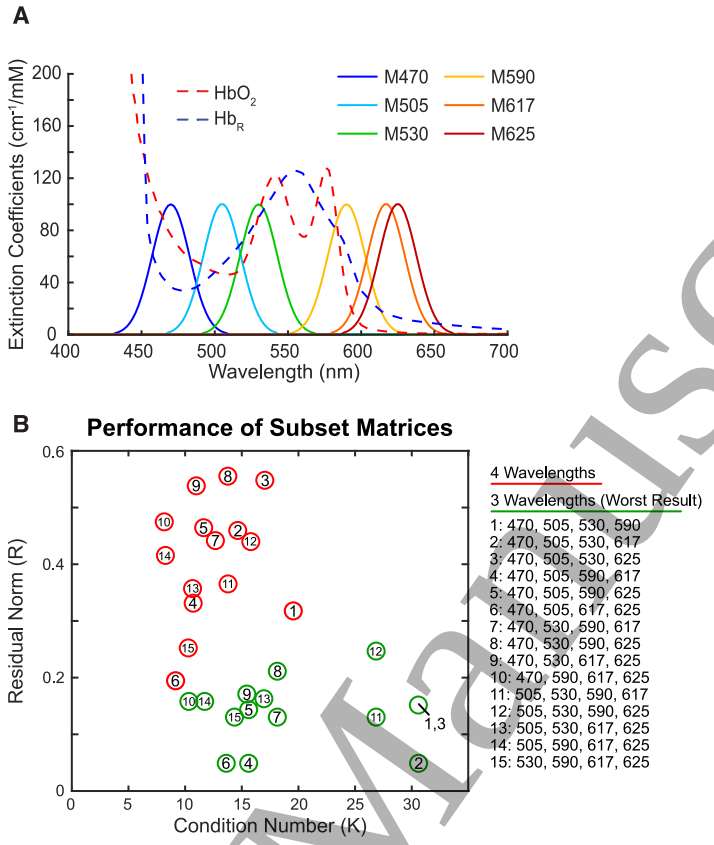

Figure 9. Theoretical performance of possible four-LED spectroscopy matrices and their three-LED sub-matrices. (A) Spectra of visible light LEDs available from ThorLabs, displayed with the extinction coefficients for oxy- and deoxyhemoglobin. (B) Theoretical performance of the full spectroscopy matrices and the worst performance of their three-LED censored subsets (combination #8 is the LEDs currently in use). Recall that better performance is expected with a high R and a low κ (*i.e.*, towards upper-left corner). Note that the matrices that perform the best as four-LED matrices (*i.e.*, the ones closest to the upper-left corner with low condition number and high residual norm) do not necessarily have the best performance with censoring of one wavelength.

other hand, for our imaging system, censoring only the green M530 LED resulted in minimal changes in results. These considerations apply most strongly to changes in oxy- and deoxyhemoglobin; interestingly, calculation of changes in the total hemoglobin concentration were less sensitive to the wavelengths preserved and were substantially more robust in the face of increased noise. Thus, while the M625 red LED was the most crucial for preserving performance in the calculation of $\Delta[\mathrm{HbO_2}]$ and $\Delta[\mathrm{Hb_R}]$, $\Delta[\mathrm{Hb_T}]$ could still be accurately determined even when that LED was censored.

Furthermore, we demonstrated that spectroscopic accuracy has direct effects on the ability to perform resting-state functional connectivity. Using wavelength censored spectroscopy, accurate correlation coefficients could still be calculated and the expected neurologic structure of functional connectivity networks could be found. As above,

analysis using $\Delta[\mathrm{Hb_T}]$ was most robust to added noise and to the loss of data. These findings connect to the results of Kura et al. (2018). They demonstrated that functional connectivity maps generated with $\Delta[\mathrm{Hb_T}]$ have higher signal-to-noise than both $\Delta[\mathrm{HbO_2}]$ and $\Delta[\mathrm{Hb_R}]$. Our work provides justification that this finding arises through experimental noise in spectroscopy rather than underlying cerebrovascular physiology. Based on their findings, to simplify data acquisition and analysis, Kura et al. propose the use of single-wavelength imaging at a wavelength sensitive to $\Delta[\mathrm{Hb_T}]$ (specifically they used the same M530 LED as in our system).

While we agree with their motivation to simplify analysis, and while our prior work also utilized single-wavelength imaging, here we have shown that use of multiple wavelengths increases experimental robustness. Our results also suggest that the error in $\Delta[\mathrm{Hb_T}]$ was lower than the added noise present in the individual wavelength data. Thus, determination of $\Delta[\mathrm{Hb_T}]$ via multi-wavelength spectroscopy is likely superior in signal-to-noise than the use of a single wavelength measurement sensitive to $\Delta[\mathrm{Hb_T}]$. Additionally, there may be situations (*e.g.*, disease models with altered neurovascular coupling) for which measuring $\Delta[\mathrm{HbO_2}]$ and $\Delta[\mathrm{Hb_R}]$ independently is important. Using multiple LEDs to over-determine the spectroscopy problem enables the use of wavelength censoring to maintain maximum flexibility in data analysis. Similarly, our methods could be extended to systems designed to measure concentration changes of water (Xiao et al. 2004) or cytochrome-C oxidase (Bale et al. 2016), which would not be possible with single-wavelength imaging.

Our results inform optimal methods for system construction, wavelength selection, and data analysis. Choosing illumination sources based on the theoretical results of the full spectroscopy matrix may not optimize for performance in the setting of data loss. We suggest following our approach to select sources based on their performance in the setting of censoring. Once a system is constructed and the performance of the spectroscopy matrix (and its censored subsets) calculated, a look-up table of acceptable wavelength combinations can be constructed for which continued analysis despite data loss is permitted.

Our experiments tested hypotheses only in the context of resting-state hemodynamics that arise through neurovascular coupling. It is possible that the anti-correlation of $\Delta[\mathrm{HbO_2}]$ and $\Delta[\mathrm{Hb_R}]$ in this setting is responsible for some of the lower noise seen with $\Delta[\mathrm{Hb_T}]$ contrast. Our simulations suggest that the robustness of $\Delta[\mathrm{Hb_T}]$ does not solely arise from this phenomenon, but we were unable to test this finding with experimental data. In the future, we plan to explore these methods using near-infrared frequency-domain or time domain systems able to calculate absolute tissue optical properties. Additionally, while detection of functional connectivity networks through correlation analysis was reasonably robust, techniques that require independent calculation of $[\mathrm{HbO_2}]$ and $[\mathrm{Hb_R}]$ to determine (for example) tissue oxygen saturation and oxygen extraction fraction may be more sensitive to experimental noise. The approaches demonstrated here are still applicable to understanding and improving spectroscopy in such contexts.

Another source of error in spectroscopy is the accuracy of the extinction coefficients in the spectroscopy matrix. If errors are made in the determination of these values, then, clearly, any spectroscopy calculations would be inaccurate. We did not address this source of error in the present study. While the tissue reduced scattering coefficient does not affect the spectroscopy matrix and algorithm directly, the diffuse pathlength is dependent on the assumed tissue absorption and reduced scattering coefficients. Errors in the calculation of the diffuse pathlength result in errors in $\mathbf{\Delta}\mu_\mathbf{a}$ and thus errors in the calculated hemoglobin concentrations. This problem has been shown to lead to crosstalk between different chromophore concentrations (Okui and Okada 2005). While outside the scope of this paper, we do intend to study the effect of error in the calculation of the diffuse pathlength in future work, especially as the scattering coefficient might be expected to vary spatially in pathology (Abookasis et al. 2009). We note, however, that simulations using both analytical solutions and Monte Carlo methods have shown that the diffuse pathlength is relatively insensitive to errors in μ_s' or μ_a in the range where our experiments were performed (Kohl et al. 2000). Thus, we expect errors from this uncertainty to be small.

In this manuscript, we only studied the effects of noise and data loss within the experimental context of OIS imaging in mice. One reason for this choice was that, in OIS, errors such as camera saturation and low signal-to-noise affect individual pixels; thus, when averaging across different subjects and imaging runs, the data loss effect is immediately visualized via reduction in field-of-view (White et al. 2019). Interestingly, similar problems arise in diffuse optical tomography (DOT) and near infrared spectroscopy (NIRS). In such human imaging systems, individual source-detector pairs may need to be censored due to low data quality (White and Culver 2010; Eggebrecht et al. 2012; Ferradal et al. 2016; Pollonini et al. 2016; Hocke et al. 2018). Such censoring needs to be accounted for accurately, for example, when visualizing data, when reconstructing three-dimensional volumes, or when statistically interpreting data. The wavelength censoring approaches we have presented (with a visible light system) are readily generalizable to the near-infrared regime used in NIRS and DOT, as long as such systems utilize more than two wavelengths. Furthermore, the algorithms could be similarly useful for other wavelengths regimes (*e.g.*, deeper infrared). Thus, our results improve the ability of optical neuroimaging and neuromonitoring to impact real-world applications based on pre-clinical and clinical subject and across multiple spectral and spatial regimes. There has been increasing optical literature on methods for removing movement artifacts from data (Cooper et al. 2012; Barker et al. 2013), and similar issues arise in functional magnetic resonance imaging (fMRI), which is very sensitive to motion artifacts (Power et al. 2012). In fMRI, volume censoring (removing time points corrupted by subject motion) has been shown to improve the data quality of functional connectivity analysis (Power et al. 2014; Siegel et al. 2014) beyond that achievable through regression of artifactual time series. As even with optimal artifact removal and filtering algorithms, censoring of data is unavoidable, statistical analysis methods that most optimally preserve the accuracy of the remaining data will become increasingly

important as translational and clinical work becomes more prevalent.

5. Conclusion

We have developed an analysis methodology and applied it to accurately perform spectroscopy even in the context of wavelength censoring. Within the context of functional neuroimaging, the use of $\Delta[\mathrm{Hb_T}]$ contrast greatly improves signal to noise and enables accurate calculations of correlations even in the setting of data loss. Calculation of $\Delta[\mathrm{HbO_2}]$ or $\Delta[\mathrm{Hb_R}]$ is more sensitive to measurement noise and loss of wavelengths, but calculation is still possible with selected subset spectroscopy matrices. Overall, these new tools and insights should improve the ability to accurately perform functional neuroimaging on individual subjects in real world experimental settings.

Funding

- National Heart Lung and Blood Institute (NHLBI) (T32-HL007915)
- National Institute of Neurological Disorders and Stroke (NINDS) (K08-NS117897)
- National Institute of Neurological Disorders and Stroke (NINDS) (R01-NS060653)
- National Institute of Biomedical Imaging and Bioengineering (NIBIB) (P41-EB015893)
- National Institute of Child Health and Human Development (NICHD) (R37-HD059288)
- Children's Hospital of Philadelphia (CHOP) Research Institute

Disclosures

Dr. White is an inventor on a patent (US9480425B2) based on the use of optical neuroimaging for resting-state functional connectivity.

References

Abookasis, D., C. C. Lay, M. S. Mathews, M. E. Linskey, R. D. Frostig, and B. J. Tromberg (2009). "Imaging cortical absorption, scattering, and hemodynamic response during ischemic stroke using spatially modulated near-infrared illumination". *J Biomed Opt* **14**, 024033.

Arifler, D., T. Zhu, S. Madaan, and I. Tachtsidis (2015). "Optimal wavelength combinations for near-infrared spectroscopic monitoring of changes in brain tissue hemoglobin and cytochrome c oxidase concentrations". *Biomed Opt Exp* **6**, 933–947.

Arridge, S. R., M. Cope, and D. T. Delpy (1992). "The theoretical basis for the determination of optical pathlengths in tissue: temporal and frequency analysis". *Phys Med Biol* **37**, 1531–1560.

Bale, G., C. E. Elwell, and I. Tachtsidis (2016). "From Jöbsis to the present day: a review of clinical near-infrared spectroscopy measurements of cerebral cytochrome-c-oxidase". *J Biomed Opt* **21**, 091307.

Barker, J. W., A. Aarabi, and T. J. Huppert (2013). "Autoregressive model based algorithm for correcting motion and serially correlated errors in fNIRS". *Biomed Opt Exp* **4**, 1366–1379.

Bauer, A. Q., A. W. Kraft, P. W. Wright, A. Z. Snyder, J.-M. Lee, and J. P. Culver (2014). "Optical imaging of disrupted functional connectivity following ischemic stroke in mice". *Neuroimage* **99**, 388–401.

Bergonzi, K. M., A. Q. Bauer, P. W. Wright, and J. P. Culver (2015). "Mapping functional connectivity using cerebral blood flow in the mouse brain". *J Cereb Blood Flow Metab* **35**, 367–370.

Bero, A. W., A. Q. Bauer, F. R. Stewart, B. R. White, J. R. Cirrito, M. E. Raichle, J. P. Culver, and D. M. Holtzman (2012). "Bidirectional relationship between functional connectivity and amyloid-β deposition in mouse brain". *J. Neurosci.* **32**, 4334–4340.

Brendel, B. and T. Nielsen (2009). "Selection of optimal wavelengths for spectral reconstruction in diffuse optical tomography". *J Biomed Opt* **14**, 034041.

Cooper, R. J., J. Selb, L. Gagnon, D. Phillip, H. W. Schytz, H. K. Iversen, M. Ashina, and D. A. Boas (2012). "A systematic comparison of motion artifact correction techniques for functional near-infrared spectroscopy". *Front Neurosci* **6**, 147.

Corlu, A., R. Choe, T. Durduran, K. Lee, M. Schweiger, S.R. Arridge, E.M.C. Hillman, and A.G. Yodh (2005). "Diffuse optical tomography with spectral constraints and wavelength optimization". *Appl Opt* **44**, 2082–2093.

Corlu, A., T. Durduran, R. Choe, M. Schweiger, E.M.C. Hillman, S.R. Arridge, and A.G. Yodh (2003). "Uniqueness and wavelength optimization in continuous-wave multi-spectral diffuse optical tomography". *Opt Lett* **28**, 2339–2341.

Correia, T., A. Gibson, and J. Hebden (2010). "Identification of the optimal wavelengths for optical topography: a photo measurement density function analysis". *J Biomed Opt* **15**, 056002.

Eggebrecht, A. T., B. R. White, S. L. Ferradal, C. Chen, Y. Zhan, A. Z. Snyder, H. Dehghani, and J. P. Culver (2012). "A quantitative spatial comparison of high-density diffuse optical tomography and fMRI cortical mapping". *Neuroimage* **61**, 1120–1128.

Ferradal, S. L., S. M. Liao, A. T. Eggebrecht, J. S. Shimony, T. E. Inder, J. P. Culver, and C. D. Smyser (2016). "Functional imaging of the development brain at the bedside using diffuse optical tomography". *Cereb. Cortex* **26**, 1558–1568.

Hillman, E. M. C. (2014). "Coupling mechanism and significance of the BOLD signal: a status report". *Annu Rev Neurosci* **37**, 161–181.

Hocke, L. M., I. K. Oni, C. C. Duszynski, A. V. Corrigan, B. deB. Frederick, and J. F. Dunn (2018). "Automated Processing of fNIRS Data–A Visual Guide to the Pitfalls and Consequences". *Algorithms* **11**, 67.

Ko, T. S. et al. (2018). "Non-invasive optical neuromonitoring of the temperature-dependence of cerebral oxygen metabolism during deep hypothermic cardiopulmonary bypass in neonatal swine". *J Cereb Blood Flow Metab* **40**, 187–203.

Kohl, M., U. Lindauer, G. Royl, M. Kühl, L. Gold, A. Villringer, and U Dirnagl (2000). "Physical model for the spectroscopic analysis of cortical intrinsic optical signals". *Phys Med Biol* **45**, 3749–3764.

Kura, S., H. Xie, B. Fu, C. Ayata, D. A. Boas, and S. Sakadzic (2018). "Intrinsic optical signal imaging of the blood volume changes is sufficient for mapping the resting state functional connectivity in the rodent cortex". *J. Neural. Eng.* **15**, 035003.

Lynch, J. M. et al. (2014). "Time to surgery and preoperative cerebral hemodynamics predict preoperative white matter injury in neonates with hypoplastic left heart syndrome". *J Thorac Cardiovasc Surg* **148**, 2181–2188.

Okui, N. and E. Okada (2005). "Wavelength dependence of crosstalk in dual-wavelength measurement of oxy- and deoxy-hemoglobin". *J Biomed Opt* **10**, 011015.

Pollonini, L., H. Bortfeld, and J. S. Oghalai (2016). "PHOEBE: a method for real time mapping of optodes-scalp coupling in functional near-infrared spectroscopy". *Biomed Opt Exp* **7**, 5104–5119.

Power, J. D., K. A. Barnes, A. Z. Snyder, B. L. Schlaggar, and S. E. Petersen (2012). "Spurious but systematic correlations in functional connectivity MRI networks arise from subject motion". *Neuroimage* **59**, 2141–2154.

Power, J. D., A. Mitra, T. O. Laumann, A. Z. Snyder, B. L. Schlaggar, and S. E. Petersen (2014). "Methods to detect, characterize, and remove motion artifact in resting state fMRI". *Neuroimage* **84**, 320–341.

Prahl, S. (2002). *Optical absorption of hemoglobin*. URL: `omlc . org / spectra / hemoglobin/summary.html`.

Raichle, M. E. (2010). "Two views of brain function". *Trend Cog Sci* **14**, 180–190.

Selb, J., M. A. Yücel, D. Phillip, H. W. Schytz, H. K. Iversen, M. Vangel, M. Ashina, and D. A. Boas (2015). "Effect of motion artifacts and their correction on near-infrared spectroscopy oscillation data: a study in healthy subjects and stroke patients". *J Biomed Opt* **20**, 056011.

Siegel, J. S., J. D. Power, J. W. Dubis, A. C. Vogel, J. A. Church, B. L. Schlaggar, and S. E. Petersen (2014). "Statistical improvements in functional magnetic resonance imaging analyses produced by censoring high-motion data points". *Hum. Brain Mapp.* **35**, 1981–1996.

Silasi, G., D. Xiao, M. P. Vanni, A. C. N. Chen, and T. H. Murphy (2016). "Intact skull chronic windows for mesoscopic wide-field imaging in awake mice". *J. Neurosci. Meth.* **267**, 141–149.

Strangman, G., M. A. Franceschini, and D. A. Boas (2003). "Factors affecting the accuracy of near-infrared spectroscopy concentration calculations for focal changes in oxygenation parameters". *Neuroimage* **18**, 865–879.

Wheelock, M. D., J. P. Culver, and A. T. Eggebrecht (2019). "High-density diffuse optical tomography for imaging human brain function". *Rev Sci Instrum* **90**, 051101.

White, B. R., A. Q. Bauer, A. Z. Snyder, B. L. Schlaggar, J.-M. Lee, and J. P. Culver (2011). "Imaging of Functional Connectivity in the Mouse Brain". *PLoS One* **6**, e16322.

White, B. R. and J. P. Culver (2010). "Phase-encoded retinotopy as an evaluation of diffuse optical neuroimaging". *Neuroimage* **49**, 568–577.

White, B. R., S. M. Liao, S. L. Ferradal, T. E. Inder, and J. P. Culver (2012). "Bedside optical imaging of occipital resting-state functional connectivity in neonates". *Neuroimage* **59**, 2529–2538.

White, B. R., J. A. Padawer-Curry, A. S. Cohen, D. J. Licht, and A. G. Yodh (2019). "Brain segmentation, spatial censoring, and averaging techniques for optical functional connectivity imaging in mice". *Biomed Opt Exp* **10**, 5952–5973.

White, B. R., A. Z. Snyder, A. L. Cohen, S. E. Petersen, M. E. Raichle, B. L. Schlaggar, and J. P. Culver (2009). "Resting-state functional connectivity in the human brain revealed with diffuse optical tomography". *Neuroimage* **47**, 148–156.

Xiao, F., J. Rodriguez, T. C. Arnold, S. Zhang, D. Ferrara, J. Ewing, D. L. Carden J. S. Alexander, and S. A. Conrad (2004). "Near-infrared spectroscopy: a tool to monitor cerebral hemodynamic and metabolic changes after cardiac arrest in rats". *Resuscitation* **63**, 213–220.

Yücel, M. A., J. J. Selb, T. J. Huppert, M. A. Franceschini, and D. A. Boas (2017). "Functional near infrared spectroscopy: enabling routine brain imaging". *Curr Opin Biomed Eng* **4**, 78–86.